

# Calcium Poly(Heptazine Imide): A Covalent Heptazine Framework for Selective CO<sub>2</sub> Adsorption

James N. Burrow, Ryan A. Ciuffo, Lettie A. Smith, Yu Wang, David C. Calabro, Graeme Henkelman, and C. Buddie Mullins\*



Cite This: *ACS Nano* 2022, 16, 5393–5403



Read Online

ACCESS |



Metrics & More



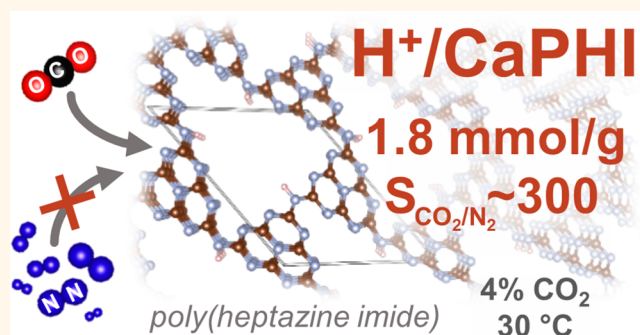
Article Recommendations



Supporting Information

**ABSTRACT:** Potassium poly(heptazine imide) (KPHI) has recently garnered attention as a crystalline carbon nitride framework with considerable photoelectrochemical activity. Here, we report a Ca<sup>2+</sup>-complexed analogue of PHI: calcium poly(heptazine imide) (CaPHI). Despite similar polymer backbone, CaPHI and KPHI exhibit markedly different crystal structures. Spectroscopic, crystallographic, and physisorptive characterization reveal that Ca<sup>2+</sup> acts as a structure-directing agent to transform melon-based carbon nitride to crystalline CaPHI with ordered pore channels, extended visible light absorption, and altered band structure as compared to KPHI. Upon acid washing, protons replace Ca<sup>2+</sup> atoms in CaPHI to yield H<sup>+</sup>/CaPHI and enhance porosity without disrupting crystal structure. Further, these proton-exchanged PHI frameworks exhibit large adsorption affinity for CO<sub>2</sub> and exceptional performance for selective carbon capture from dilute streams. Compared to a state-of-the-art metal organic framework, UTSA-16, H<sup>+</sup>/CaPHI exhibits more than twice the selectivity (~300 vs ~120) and working capacity (~1.2 mmol g<sup>-1</sup> vs ~0.5 mmol g<sup>-1</sup>) for a feed of 4% CO<sub>2</sub> (1 bar, 30 °C).

**KEYWORDS:** covalent organic frameworks, carbon nitride, organic semiconductors, gas adsorption, carbon capture



Applications benefiting from extensive interfacial contact in catalysis, separations, and energy storage have prompted the discovery and design of functional nanoporous materials, such as ordered metal–organic frameworks (MOFs) and amorphous activated carbons (ACs). Between these two extremes of designer nanoporous materials resides the relatively newer materials class of covalent organic frameworks (COFs), pioneered by Côté, Yaghi et al. in 2005.<sup>1</sup> As porous, crystalline polymers linked exclusively by covalent bonds, COFs combine the merits of a well-defined framework intrinsic to MOFs with the inherent physicochemical stability of ACs. Seminal work in 2008 by Kuhn, Antonietti, and Thomas showed that COFs based on triazine nodes, frequently dubbed ‘covalent triazine frameworks’ (CTFs), can easily be accessed via ionothermal routes.<sup>2</sup> To date, CTFs have already shown impressive performance as robust sensors, catalyst supports, adsorbents, and metal-free photo(electro)catalysts.<sup>3,4</sup>

In 2017, work by Zhang et al. extended this subclass of CTFs to allow heptazine (tris-*s*-triazine) nodes by reporting an ionic carbon nitride allotrope consisting of a negatively charged poly(heptazine imide) (PHI) anion framework balanced by potassium (K<sup>+</sup>) cations.<sup>5</sup> Since its discovery, KPHI has been

investigated extensively as a photocatalyst for solar hydrogen production and for organic synthesis thanks to its ability to store light in the form of long-lived radicals even under dark conditions.<sup>6</sup> Schlomberg et al. completed an in-depth study of the polymeric and crystallographic structure of KPHI,<sup>7</sup> and Chen, Savateev et al. further showed the propensity of KPHI to undergo ion exchange with protons and various metal cations with preservation of the original KPHI crystal structure.<sup>8,9</sup> Interestingly, upon exchange with divalent calcium cations (Ca<sup>2+</sup>), the crystalline structure was lost, yet the amorphous CaPHI showed improved photocatalytic performance. Further work by Sahoo, Kühne et al. showed that replacing K<sup>+</sup> with magnesium cations (Mg<sup>2+</sup>) through a simple aqueous ion exchange process could also alter the band structure by

Received: October 9, 2021

Accepted: March 18, 2022

Published: March 31, 2022



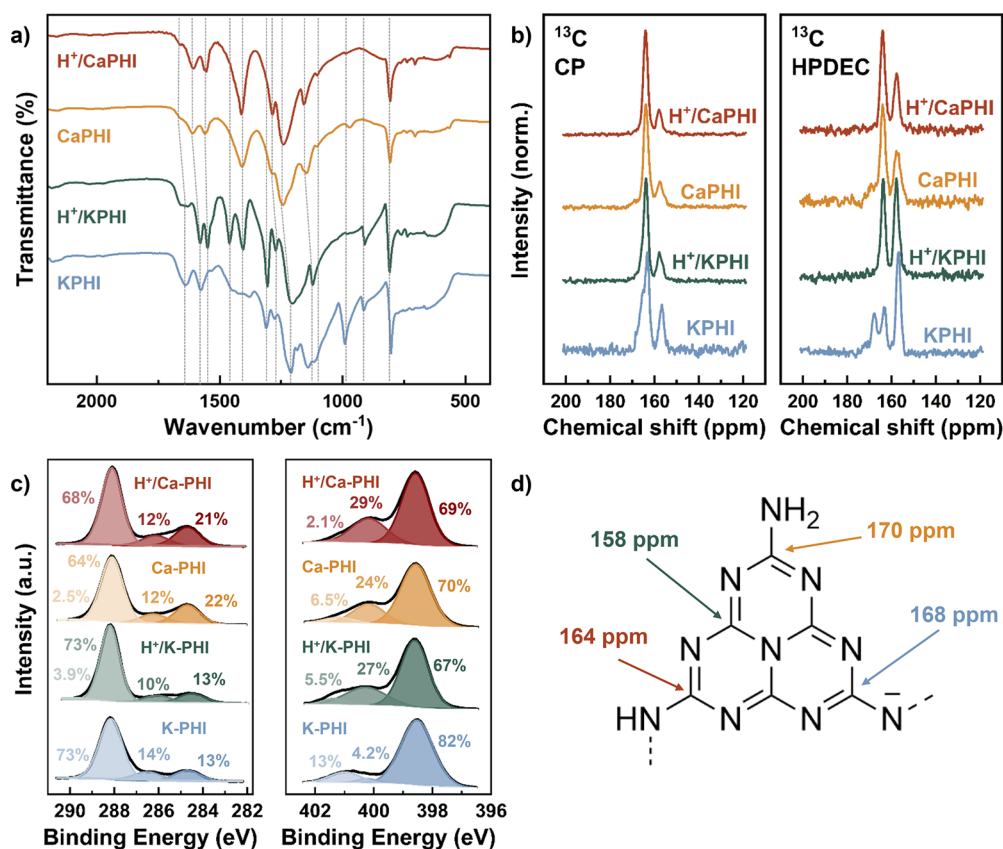


**Figure 1.** Spectroscopic characterization of the polymeric backbone of the Ca- and KPHI materials, including (a) ATR-FTIR; (b)  $^{13}\text{C}$  MAS NMR in CP mode and HPDEC mode; (c) high-resolution XPS scans of the C 1s and N 1s regions; and (d) proposed polymeric structure.

lowering the valence band maximum toward more oxidizing positions, effectively enabling overall water splitting.<sup>10</sup>

Recently, our group reported the synthesis of N-rich nanoporous carbons for selective  $\text{CO}_2$  adsorption by calcium chloride ( $\text{CaCl}_2$ ) mediated ionothermal treatment of melon-based carbon nitride.<sup>11</sup> In doing so, we discovered the conversion toward a semicrystalline intermediate just before the onset of carbonization. In the current work, we report an optimized salt melt synthetic process for isolating this crystalline framework, a Ca-complexed analogue of PHI with altered crystalline structure as compared to KPHI. With MAS NMR, (ATR-)FTIR, XPS, UPS, (DR-)UV-vis, XRD, SEM, TEM,  $\text{N}_2$  physisorption, and elemental analysis supported by theoretical modeling, we show that  $\text{Ca}^{2+}$  acts as bridging and structure-directing agent to transform melon-based carbon nitride to CaPHI, a nanoporous framework material. Compared to the previously reported KPHI, CaPHI has a similar polymeric backbone but significantly altered crystalline structure with more lattice strain, likely due to differences in valence and ionic radius of the templating cation. The cations reside in charged pockets within the crystal structure, interacting with pyridinic N species for stabilization and with deprotonated bridging secondary amines between heptazine units for charge balance. While the layered structure of both materials results in pore columns filled with framework-complexed cations, the geometry of the triangular-shaped pores elongated and flexed when accommodating  $\text{Ca}^{2+}$  compared to  $\text{K}^+$ . Upon acid washing, protons replace  $\text{Ca}^{2+}$  atoms in the  $\text{CaCl}_2$ -derived PHI material to yield  $\text{H}^+$ /CaPHI with enhanced porosity and surface area without significantly altering the crystal structure from its parent CaPHI material.

This exciting carbon nitride framework material has ordered pore channels, extended visible light absorption, and altered band structure with similar textural properties and crystalline size to the recently exploited KPHI, suggesting that CaPHI may be useful in photoelectrocatalysis. Importantly, these proton-exchanged PHI carbon nitride allotropes exhibit large affinity for  $\text{CO}_2$  adsorption and show propensity for selective carbon capture from dilute streams.

## RESULTS AND DISCUSSION

Both KPHI and CaPHI were synthesized via a salt melt route. Treatment with HCl allowed quantitative replacement of the framework-complexed cations with protons. For clarity, materials obtained by acid-washing KPHI and CaPHI will be referred to as  $\text{H}^+$ /KPHI and  $\text{H}^+$ /CaPHI, respectively, for the remainder of this manuscript; this notation is not meant to denote a partial exchange of cations with protons, but instead emphasizes the parent structure from which the completely protonated analogues were derived. After isolating the crystalline ( $\text{H}^+$ )/CaPHI carbon nitride allotrope, the chemical structure of the polymeric backbone was first investigated with Fourier-transformed infrared spectroscopy in attenuated total reflectance mode (ATR-FTIR). Informed by the seminal work of Savateev et al.,<sup>9</sup> ATR-FTIR revealed that CaPHI was composed of a similar polymeric backbone as the previously investigated KPHI. The spectra, shown in Figure 1a, show peaks at  $800\text{ cm}^{-1}$  that are characteristic of heptazine (e.g., tris-triazine) subunits for both Ca- and KPHI (and their proton-exchanged) analogues. Fingerprint peaks in the  $1100\text{--}1500\text{ cm}^{-1}$  region correspond to the C—N and C=N bonding

modes, and peaks near 1575 and 1650  $\text{cm}^{-1}$  come from N—H bending modes in protonated primary and secondary amines ( $\text{H}_2\text{NC}$  and  $\text{HNC}_2$ ) that serve as terminating and linking motifs, respectively. Weak peaks around 2150  $\text{cm}^{-1}$  correspond to cyano ( $\text{C}\equiv\text{N}^-$ ) groups, and broad peaks at wavenumbers greater than 3000  $\text{cm}^{-1}$  corroborate the presence of amines ( $-\text{NH}_2$ ) or surface-hydroxyl ( $-\text{OH}$ ) groups stemming from aqueous workup. Additionally, a peak near 1000  $\text{cm}^{-1}$  is associated with the cation- $\text{NC}_2$  binding in the K- and CaPHI materials, and this peak disappears upon acid washing and protonation of the bridging imines. The cation- $\text{NC}_2$  features also seemed much stronger for KPHI as compared to CaPHI, which suggests a larger quantity of cation-complexes in KPHI. While there are slight vibrational shifts in the fingerprint regions between Ca- and K-derived materials, the most notable disparities between the set of frameworks stem from the relative intensities of binding modes associated with amines, suggesting that the main differences between the backbones of these two classes of materials were the proportion and type of amines present. CaPHI showed a greater ratio of intensity for protonated secondary vs primary amines. Since cation-complexed (i.e., unprotonated) linking amines would not contribute to IR signal intensity, this change in observed intensity ratio could further suggest that a larger proportion of the linkage amine groups were protonated (i.e., not complexed to a cation) in CaPHI than in KPHI.

For further, more precise analysis of the polymeric connectivity of these PHI frameworks, solid-state carbon and nitrogen nuclear magnetic resonance ( $^{13}\text{C}$ -,  $^{15}\text{N}$ -MAS NMR) was employed. In agreement with work by Schlomberg et al.,<sup>7</sup> the  $^{13}\text{C}$  MAS NMR response of the KPHI material showed four distinct types of carbons evidenced by two strong peaks and a weak shoulder in cross-polarization mode, and three distinct peaks with a weak shoulder in the proton-decoupled, direct-excitation mode (Figure 1b). The peak with a chemical shift of 158 ppm corresponded to the heptazine-type carbon within the heptazine-subunits, while the peaks at 164 and 168 ppm were related to carbons neighboring protonated vs cation-complexed N species, respectively. The weaker shoulder with largest chemical shift near 170 ppm was indicative of carbons bound to terminating, primary amines. Acid washing resulted in the removal of the cation-complexed peak at 168 ppm as the intensity of the peak corresponding to protonated N species increased. Though solid-state NMR is not quantitative, the proton-decoupled experiments (HPDEC) serve as a rough estimate, and quantification of these spectra can be found in SI Table S7. The only discernible differences in the  $^{13}\text{C}$  MAS NMR response between the Ca- and the KPHI materials came from differences in the relative intensity of the peaks at 158 and 164 ppm, which could suggest that a proportion of the pyridinic-type N in the heptazine rings of CaPHI could have been protonated. This is further demonstrated by the  $^{15}\text{N}$  MAS NMR spectra (SI Figure S1); under the same experimental conditions during cross-polarization, CaPHI materials showed both increased overall intensity and a larger protonated:pyridinic ratio, which suggests a larger proton concentration near N species. Overall, though, these MAS NMR results show further concrete evidence of the chemical similarity of the polymeric backbone of the Ca- and KPHI materials.

Further, bulk elemental analysis (CHN EA) and X-ray photoelectron spectroscopy (XPS) provided quantitative evidence for the chemical similarity between the Ca- and KPHI materials. XPS analysis of all PHI frameworks showed

peaks in the C 1s region at 284.7, 286.2, and 288.3 eV, corresponding to adventitious carbon (C—C), aminated or hydroxylated carbons (C— $\text{NH}_x$ /C—O), and heptazine ring-type carbons ( $\text{CN}_3$ ), respectively. For CaPHI and  $\text{H}^+$ /KPHI, a small amount of signal near 290 eV corresponding to oxidized carbons (C=O) was also detected. For the N 1s region, peaks were observed at 398.5, 400.2, and 401.3 eV, corresponding to pyridinic ring-type nitrogen (C— $\text{N}=\text{C}$ ), central heptazine nitrogen ( $\text{NC}_3$ ), and amines ( $\text{NH}_x$ ), respectively. Additionally, the C 1s and N 1s region of all samples showed a  $\pi$ — $\pi^*$  shakeup feature commonly observed for conjugated systems shifted about 5 eV from the major peak (besides KPHI, for which the K 2p region overlaps with this feature). Survey scans (SI Figure S2) and integration of high-resolution XPS spectra (Figure 1c and SI Figure S3) revealed that KPHI had surface compositions of 36 at% C, 37 at% N, 24 at% K, and 3.4 at% O, yielding a total molar N/C ratio of 1.03. Proton-exchanged  $\text{H}^+$ /KPHI was composed of 48 at% C, 49 at% N, 3.5 at% O, and no residual K detectable by XPS, with an N/C ratio of 1.02 in good agreement with the value observed for the  $\text{K}^+$ -complexed framework. For CaPHI, XPS indicated a surface composition of 49 at% C, 44 at% N, 5.7 at% O, and only 1 at% Ca after workup, suggesting a slightly smaller N/C ratio of 0.90 and many fewer remaining  $\text{Ca}^{2+}$  cations as compared to KPHI. XPS analysis of acid-treated  $\text{H}^+$ /CaPHI revealed a surface composition of 49 at% C, 45 at% N, 5.8 at% O, and trace amounts of Ca detectable, yielding an observed N/C ratio of 0.92 similar to that of the water-washed CaPHI.

These surface N/C ratios for both  $\text{Ca}^{2+}$ - and  $\text{K}^+$ -derived samples observed by XPS were much lower than the theoretical value derived from the expected poly(heptazine imide) structure, which ranges from about 1.33 to 1.67 depending on the number of repeat units in the lateral sheets and the nature of terminating groups (e.g., primary amines or cyanides). Deviations from this expected N/C ratio observed by XPS likely stemmed from adventitious carbon impurities on the surface of these materials, which contribute to the C 1s peaks at 284.7, 286.2, and 290 eV and account for nearly a third of all detected C species on the surface. On the other hand, when comparing the N content only to the amount of carbon in the heptazine configuration at 288.3 eV (as expected for pure PHI), the N/C ratio is closer to 1.4 for all synthesized materials, which falls in the expected range. Additionally, the presence of O in these materials is assumed to derive from small levels of surface oxidation and tightly bound water. On the other hand, CHN EA of the bulk (summarized in SI Table S1) indicated a molar N/C ratio of 1.42 and 1.41 for ( $\text{H}^+$ /)KPHI and ( $\text{H}^+$ /)CaPHI, respectively, reconfirming the chemical similarity between these two materials. This bulk N/C ratio is much closer to the expected stoichiometry of a melem- ( $\text{C}_6\text{N}_{10}\text{H}_6$ , N/C = 1.67) based polymer and falls in line with previous results by Schlomberg et al. to support the conclusion that these framework materials are composed of poly(heptazine imide) polymers.<sup>7</sup> Additionally, the H contents of the acid-washed frameworks estimated from CHN EA were nearly identical, but the water-washed KPHI showed about half the H content as compared to CaPHI (SI Table S1).

This difference in H content points toward the major chemical difference between Ca- and KPHI: the proportion of cations remaining after aqueous workup. Indicators of cation-complexed imides (e.g., IR peak near 1000  $\text{cm}^{-1}$  and  $^{13}\text{C}$  chemical shift at 168 ppm) were much stronger for KPHI than for CaPHI. XPS quantification showed cation:N ratios of 0.64

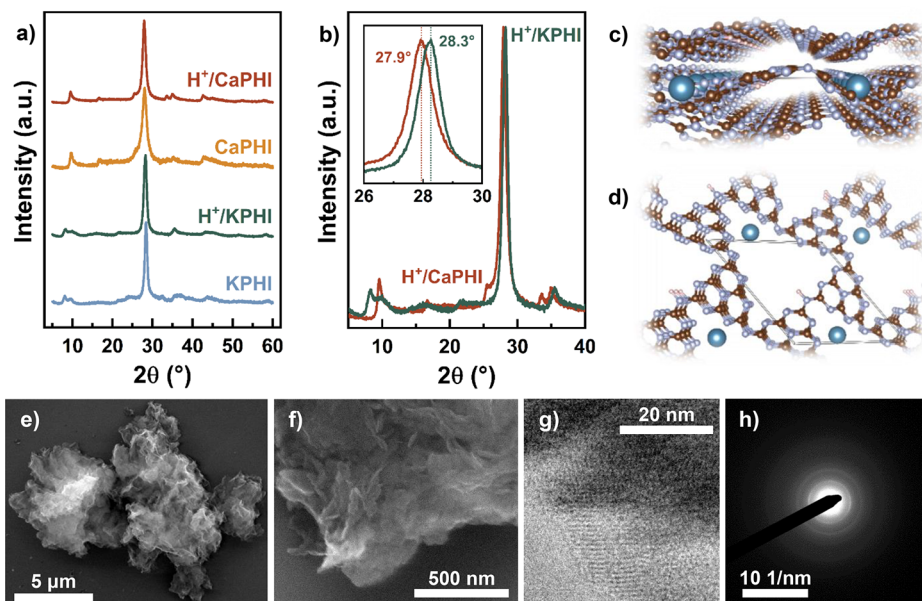


**Figure 2.** Structural characteristics of the PHI materials as determined by (a) and (b) PXRD, DFT structure relaxation of CaPHI with in-plane (c) and top-down (d) views, SEM of H<sup>+</sup>/CaPHI (e,f), (g) HRTEM of H<sup>+</sup>/CaPHI, and (h) SAED of polycrystalline H<sup>+</sup>/CaPHI.

for KPHI but only 0.02 for CaPHI. This discrepancy is much too large to be explained by charge-balance alone, so a large proportion of the imide-complexed Ca<sup>2+</sup> cations were likely displaced by protons during water washing. Additionally, as XPS is a surface sensitive technique, the cation concentration in the top few nanometers of the PHI particles could have been much smaller than the bulk. To more closely investigate the cation content of the bulk PHI frameworks, inductively coupled plasma mass spectrometry (ICP-MS) was employed, and the results are summarized in SI Table S2. These studies suggested that KPHI exhibited around 17 wt % K<sup>+</sup>, implying a charge-balanced structural formula close to (C<sub>12</sub>N<sub>17</sub>)<sub>3</sub>K<sub>6</sub>H<sub>3</sub>. On the other hand, CaPHI exhibited only 6.4 wt % Ca<sup>2+</sup>, suggesting a formula of (C<sub>12</sub>N<sub>17</sub>)<sub>3</sub>Ca<sub>2</sub>H<sub>5</sub>. This difference in extent of proton exchange could have been caused by changes in the pK<sub>a</sub> of the resulting polymeric backbones.<sup>9</sup> Further investigation of the acid–base characteristics of these PHI materials was achieved via potentiometric titration experiments, and discussion can be found in the SI.

Despite the close chemical similarity in polymeric backbone, the Ca<sup>2+</sup>- and K<sup>+</sup>-derived PHI frameworks exhibited very different crystal structures, pointing toward the structure-directing nature of the divalent CaCl<sub>2</sub> melt. As shown in Figure 2a,b, the PXRD pattern of (H<sup>+</sup>/)CaPHI shows a different response as compared to the well-studied (H<sup>+</sup>/)KPHI structure. As reported by Schlomberg et al., KPHI exhibits a pseudo-hexagonal structure with  $a = b = 12.78 \text{ \AA}$ ,  $c = 4.31 \text{ \AA}$ ,  $\alpha = \beta = 109.63^\circ$ ,  $\gamma = 120^\circ$ , and a resulting unit cell volume of 451.4 Å<sup>3</sup>.<sup>7</sup> In contrast, DFT modeling of the Ca<sup>2+</sup>-complexed PHI framework and subsequent structure relaxation suggested that (H<sup>+</sup>/)CaPHI crystallizes as a strained, triclinic lattice with  $a = 12.62 \text{ \AA}$ ,  $b = 12.02 \text{ \AA}$ ,  $c = 4.33 \text{ \AA}$ ,  $\alpha = 95.52^\circ$ ,  $\beta = 126.16^\circ$ ,  $\gamma = 117.56^\circ$ , and a slightly smaller unit cell volume of 403.0 Å<sup>3</sup>. The main difference in these two crystal structures is manifested by the apparent corrugation of the sheets in the CaPHI allotrope; while KPHI crystallizes predominantly in stacked, 2-D sheets of poly(heptazine imides), CaPHI exhibits significant disruption to this perfectly planar structure as

shown in Figure 2c. A side-by-side comparison of the predicted crystal structures for CaPHI and KPHI can be found in SI Figure S15.

These differences in crystal structure, despite chemical similarity of the backbone, are likely related to the difference in ionic radius (152 pm for K<sup>+</sup> vs 114 pm for Ca<sup>2+</sup>), more than doubled charge to radius ratio, valence, and resulting Lewis acidity of the framework-complexed cations. While K<sup>+</sup> ions interact predominantly with a single layer of the sheet-like PHI, the much more polarizing Ca<sup>2+</sup> ions interact with as many as three PHI sheets, acting as bridging moieties. This heightened interaction of the Ca<sup>2+</sup> sites with Lewis base sites on neighboring PHI sheets is present during structure assembly. To accommodate this difference in the templating cation, the crystal structure flexes in the *ab* plane and expands slightly along the *c*-axis as evident by the shift of the 002 peak in Figure 2b from ~28.3° to ~27.9°, corresponding to *d*-spacings of 3.14 and 3.19 Å in H<sup>+</sup>/KPHI to H<sup>+</sup>/CaPHI, respectively. Scherrer analysis on this 002 reflection of the synthesized H<sup>+</sup>/CaPHI and H<sup>+</sup>/KPHI indicated comparable average crystallite sizes of 8.7 and 11.4 nm, respectively, along the *c*-axis (SI Table S3). This disrupting in the planar crystal structure of CaPHI compared to KPHI might be the cause of the loss of crystallinity upon exchange of K<sup>+</sup> with Ca<sup>2+</sup> previously observed by Savateev et al.; once the sheets stack in a planar fashion, they likely cannot easily flex to accommodate Ca<sup>2+</sup>.<sup>9</sup> However, despite the apparent disruption in planarity of the PHI sheets, the CaPHI structure exhibits a similar stacking motif to the previously studied KPHI, where heptazine units align along the *c*-axis to form an ordered pore channel filled with the templating cation, Ca<sup>2+</sup>. This feature of the PHI family is in stark contrast to most allotropes of carbon nitride, such as the popular graphitic carbon nitride (g-C<sub>3</sub>N<sub>4</sub>). The fully condensed g-C<sub>3</sub>N<sub>4</sub> differs from PHI materials in that there are no bridging amines between heptazine monomers, resulting in an AB stacking motif and an absence of ordered pore channels.

Though both PHI allotropes exhibit these pore channels, the exact geometry of the triangular pores was altered when the

templating cation was changed from  $K^+$  to  $Ca^{2+}$ . While KPHI exhibits an equilateral triangular pore geometry with dimensions close to 1.34 nm on each side, CaPHI instead exhibits an isosceles geometry with dimensions of  $1.32 \times 1.32 \times 1.39$  nm due to the increased intralayer strain apparently required to accommodate the more polarizing, charge-dense  $Ca^{2+}$  cation. Furthermore, these differences in crystal structure and pore architecture, determined by the templating cation, are retained even after cation removal via acid washing;  $H^+/CaPHI$  exhibits nearly identical XRD pattern as CaPHI, and  $H^+/KPHI$  shows almost the same XRD pattern as does KPHI. At the high temperature, molten salt-mediated synthesis environment during which the parent structures are formed, the frameworks are more labile, and the individual sheets are more able to accommodate the different charge densities of  $Ca^{2+}$  vs  $K^+$ . However, upon cooling, the frameworks have less thermal motion/mobility and are likely kinetically trapped in the phases originally determined by the templating cation, even after protonation. These conclusions are supported by thermogravimetric analysis results (SI Figure S16), where the decomposition of Ca-derived frameworks seems to occur at lower temperatures, indicating slightly less stability than their K-derived counterparts.

Electron microscopy was employed to further investigate the  $H^+/CaPHI$  carbon nitride framework. Scanning electron microscopy (SEM) revealed that the bulk  $H^+/CaPHI$  exhibits a morphology of micron-sized secondary particles (Figure 2e) of primary aggregated platelet-like nanocrystals (Figure 2f). Closer inspection with low-dose HRTEM (Figure 2g) and subsequent electron diffraction imaging (Figure 2h) confirmed the lattice spacing of the polycrystalline  $H^+/CaPHI$  framework material. An intensity scan across the lattice lines observed with HRTEM, shown in SI Figure S4, corroborates the crystalline nature of these materials, showing periodicity that correlates well with  $d$ -spacing of the 002 reflection extracted from PXRD measurements. The diffuse rings observed via electron diffraction in Figure 2h stem from the polycrystalline nature of the secondary particles, and the location of these rings agree well with the predominant peaks observed in PXRD.

The optoelectronic properties of these two different carbon nitride allotropes varied significantly as a result of the altered crystalline structure and morphology. The band structure (Figure 3d) of CaPHI, KPHI, and  $H^+$ -exchanged counterparts was quantified with diffuse reflectance UV–vis spectroscopy (DRUV–vis) (Figure 3a) and ultraviolet photoelectron spectroscopy (UPS) (Figure 3c). In contrast to KPHI and  $H^+/KPHI$ , which show relatively sharp absorption onsets near 450 nm, CaPHI and  $H^+/CaPHI$  exhibit at least two different electronic transitions. Further insight was extracted from DRUV–vis data by employing analysis proposed by V. Kumar et al. to quantify the band gaps in these PHI materials (Figure 3b).<sup>12</sup> The measured optical band gaps for KPHI and  $H^+/KPHI$  were 2.72 and 2.93 eV, respectively. CaPHI and  $H^+/CaPHI$ , alternatively, showed comparatively larger band gaps of 2.82 and 3.07 eV. In each case, ion exchange of the frameworks led to  $\sim 0.2$  eV increase in the observable band gaps. This primary transition was associated with the  $\pi$ – $\pi^*$  transition in the conjugate heptazine moiety as previously observed by Sahoo, Kühne et al.<sup>10</sup> Additionally the  $Ca^{2+}$ -derived materials showed evidence of additional electronic transitions of 2.21 eV for CaPHI and 2.43 eV for  $H^+/CaPHI$  that are likely associated with additional  $n$ – $\pi^*$  transitions

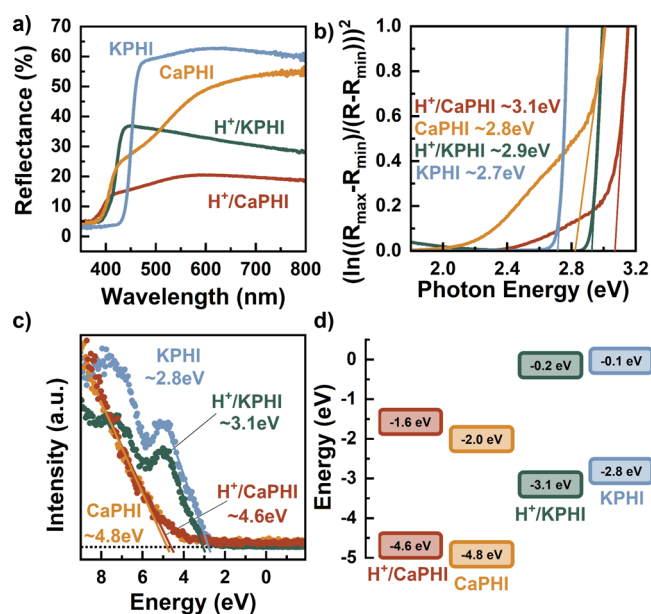


**Figure 3.** Quantification of optoelectronic properties by (a) diffuse reflectance ultraviolet–visible spectroscopy (DRUV–vis), (b) optical band gap determination, (c) ultraviolet photoelectron spectroscopy (UPS), and (d) conduction and valence band positions on the physical scale.

involving the lone pair of pyridinic N atoms, accessible due to the corrugation of the PHI sheets.<sup>13,14</sup> Similar states residing within the bandgap were observed to a lesser extent for KPHI by Savateev et al. associated with slight disorder and flexibility in the planar arrangement that allowed for out-of-plane conformations.<sup>15</sup> While DRUV–vis data here shows a slight indication of these intraband states for KPHI (e.g., small absorption onset near 600 nm), these transitions were not as prevalent as in CaPHI or  $H^+/CaPHI$  and seem to be totally absent in  $H^+/KPHI$ . With UPS, the valence band positions of these PHI materials were also estimated (Figure 3c). KPHI and  $H^+/KPHI$  showed an onset of photoelectron emission at 2.79 and 3.12 eV, and CaPHI and  $H^+/CaPHI$  exhibited valence positions around 4.84 and 4.64 eV, respectively. Further confirmation of  $n$ – $\pi^*$  transitions in CaPHI and  $H^+/CaPHI$  is evident in the UPS data, with gradual onsets occurring at energies around 3.4 eV. Combined with the extracted optical band gaps, the information on the valence band positions allowed an estimation of the band structure of the PHI class of materials (Figure 3d). This relative comparison of the optoelectronic structure between the various allotropes of PHI frameworks demonstrates that despite similar polymeric backbone, the corrugated and compressed crystalline structure associated with  $Ca^{2+}$ -templating shifted the bands of CaPHI and  $H^+/CaPHI$  toward more oxidizing positions than the more planar KPHI structure.

Textural properties of the various synthesized carbon nitride framework materials were quantified with  $N_2$  porosimetry. All of KPHI, CaPHI, and their proton-exchanged analogues exhibited a convolution of Type I and Type IV isotherm shapes with H4 hysteresis (Figure 4a), indicating a hierarchical pore structure composed of both micro- and mesopores. After proper point selection, BET analysis (SI Figure S5) revealed that, despite similar average primary crystallite sizes, the surface area of CaPHI ( $43.5 \text{ m}^2 \text{ g}^{-1}$ ) was more than three times smaller than the surface area of KPHI ( $152 \text{ m}^2 \text{ g}^{-1}$ ).

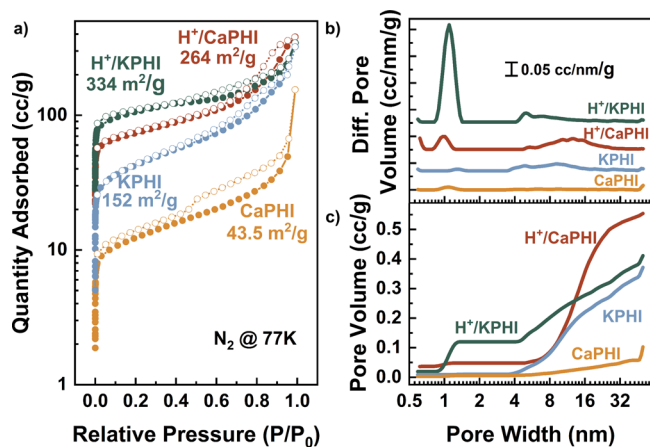


**Figure 4.** Surface area and porosity as quantified by (a)  $N_2$  isotherms at 77K and the resulting QSDFT-derived (b) pore size distributions and (c) cumulative pore volumes.

These differences therefore likely stem from differences in the secondary particle size, as larger particles would be associated with a smaller external  $N_2$ -accessible surface area. As visible in the extracted pore size distributions in Figure 4b,c, these cation-complexed frameworks exhibited near negligible microporosity ( $<0.01 \text{ cc g}^{-1}$ ), and most of the surface area was composed of mesopores larger than 4 nm, likely due to stacking faults between the primary nanocrystals that comprised the micron-sized particles. However, upon removal of  $Ca^{2+}$  or  $K^+$  via washing with acid, the interior pore channels of these frameworks were accessible for  $N_2$  adsorption, and the BET surface area increased to  $264 \text{ m}^2 \text{ g}^{-1}$  and  $334 \text{ m}^2 \text{ g}^{-1}$  for  $H^+/CaPHI$  and  $H^+/KPHI$ , respectively. Pore size distributions (Figure 4b) revealed that a considerable amount of microporosity was generated in both PHI allotropes after acid washing. As evident in Figure 4c,  $H^+/CaPHI$  exhibited almost twice as much ultramicroporosity as  $H^+/KPHI$ , with nearly  $0.04 \text{ cc g}^{-1}$  of pores with width less than 0.7 nm. This increase in volume of these narrow pores has been shown to be critical for enhanced low-pressure  $CO_2$  uptake and was likely associated with the altered crystalline structure of  $H^+/CaPHI$  as compared to  $H^+/KPHI$ . On the other hand,  $H^+/KPHI$  exhibited more than  $0.12 \text{ cc/g}$  of micropores ( $<2 \text{ nm}$ ), with most having a width of 1 nm. In addition to this increase in micropore volume and BET surface area, proton exchange was also associated with a large increase in volume of larger mesopores ( $>4 \text{ nm}$ ) for both allotropes, with the total measured porosity of  $H^+/CaPHI$  exceeding  $0.5 \text{ cc g}^{-1}$ . Overall, while the cation-complexed frameworks exhibited moderate external surface areas stemming from the secondary particle agglomerations, acid-washed counterparts  $H^+/CaPHI$  and  $H^+/KPHI$  showed that the cation exchange for much smaller protons allowed  $N_2$  to access at least a portion of the inner porosity of the ordered pore channels formed by the stacked PHI sheets.

Due to this accessible (ultra)microporosity associated with the ordered pore channels coupled with a dipole-rich structure and surface chemistry from polymeric backbone, both  $H^+/CaPHI$  and  $H^+/KPHI$  were investigated as  $CO_2$  adsorbents for application in carbon capture and gas separation.<sup>16</sup> As shown in Figure 5a, variable temperature isotherms were measured for both carbon nitride frameworks. Both  $H^+/CaPHI$  and  $H^+/KPHI$  show similar isotherm shapes with steep uptakes at

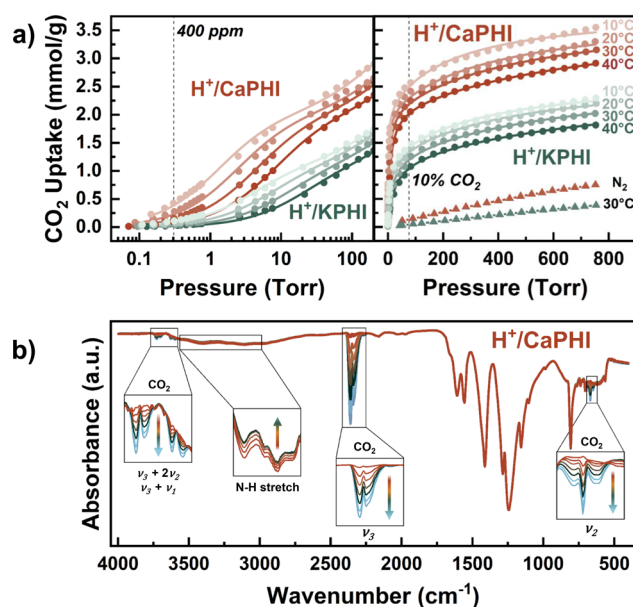


**Figure 5.** Interactions of  $CO_2$  with the proton-exchanged PHI frameworks as quantified by (a) variable temperature isotherms at lower (left) and higher (right) pressures and (b) time-resolved in situ ATR-FTIR.  $N_2$  uptakes at  $30^\circ\text{C}$  are shown as triangles, and temperature- and pressure-dependent dual-site Langmuir fits for the  $CO_2$  isotherms are shown as solid lines in (a).

pressures below 100 Torr followed by a gradual plateau near atmospheric pressure. The steep uptakes at low pressures are reminiscent of  $CO_2$  adsorption in zeolites (e.g.,  $NaX^{17}$ ), MOFs (e.g.,  $Mg_2(\text{dobdc})^{18}$ ), and solid-tethered amines (e.g.,  $PEI/SBA-15^{19}$ ), indicative of strong interactions of  $CO_2$  with the PHI frameworks. Despite similarity in isotherm shape, the magnitude of  $CO_2$  uptake was nearly twice as much in the  $Ca^{2+}$ -derived material compared to the previously reported  $K^+$ -derived framework.

For further quantitative comparison between these two carbon nitride frameworks, the various isotherms for  $H^+/CaPHI$  and  $H^+/KPHI$  were fit to dual site Langmuir (DSL) models, and a van't Hoff (i.e., Arrhenius) relation was employed to capture temperature dependence and extract thermodynamic parameters.<sup>20</sup> Eqs 1 and 2 below show the parameters that were included in this model, and more detailed information can be found in the SI.

$$q = q_A + q_B = \frac{q_{A,\text{sat}} b_A P}{(1 + b_A P)} + \frac{q_{B,\text{sat}} b_B P}{(1 + b_B P)} \quad (1)$$

$$K_i = b_i RT = \exp\left(\frac{\Delta S_{\text{ads},i}}{R}\right) \times \exp\left(\frac{-\Delta H_{\text{ads},i}}{RT}\right) \quad (2)$$

As shown in Figure 5a, the DSL model fits the observed data with excellent accuracy ( $\text{Adj. } R^2 > 0.999$ ) for both samples across all temperatures, even at very low pressures. Extracted fitting parameters are tabulated in the SI and are discussed in detail below. Heat maps in SI Figure S6 show how this dual site analysis enabled predictive quantification of the  $CO_2$  uptake over a wide range of temperatures and pressures, which is useful for process modeling and optimization. Additionally, temperature-dependent analysis allows comparison not only of the adsorption site saturation capacities ( $q_i$ )

but also the enthalpy and entropy changes ( $\Delta H_{\text{ads},i}$  and  $\Delta S_{\text{ads},i}$ ) associated with the adsorption of  $\text{CO}_2$ .

The steep uptake at low pressures can be described by adsorption in the primary adsorption site ( $q_A$ ), and the gradual uptake across higher pressures is associated with the secondary adsorption site ( $q_B$ ). The saturation capacity of the primary site,  $q_{A,\text{sat}}$  was nearly two times as large for  $\text{H}^+/\text{CaPHI}$  as compared to  $\text{H}^+/\text{KPHI}$  (2.1 vs 1.2 mmol  $\text{g}^{-1}$ ). For the secondary site,  $\text{H}^+/\text{CaPHI}$  also exhibited a larger saturation capacity ( $q_{B,\text{sat}}$ ) than did  $\text{H}^+/\text{KPHI}$  (1.8 vs 1.5 mmol  $\text{g}^{-1}$ ). These larger saturation capacities for  $\text{H}^+/\text{CaPHI}$  could be related to the larger ultramicropore volume, which has been shown to be of critical importance for  $\text{CO}_2$  adsorption,<sup>21</sup> of  $\text{H}^+/\text{CaPHI}$  as compared to  $\text{H}^+/\text{KPHI}$  as visible in Figure 4c. These changes in the ultramicropore volume, as discussed previously, are likely related to the altered crystalline structure of  $\text{H}^+/\text{CaPHI}$  as compared to  $\text{H}^+/\text{KPHI}$ .

While the adsorption saturation capacities between the two carbon nitride frameworks were very different, the energetics of adsorption were more comparable, which is indicative of similar modes of adsorption likely due to the analogous composition and surface chemistry of the two PHI materials. For  $\Delta H_{\text{ads},i}$  in both  $\text{H}^+/\text{CaPHI}$  and  $\text{H}^+/\text{KPHI}$ , the primary site exhibited an enhancement of nearly 15 kJ  $\text{mol}^{-1}$  as compared to the secondary site, which helps to explain the order of magnitude difference in the pressure-response between these two sites. Despite this similarity between the materials,  $\text{H}^+/\text{CaPHI}$  did however exhibit about 5 kJ  $\text{mol}^{-1}$  increase in affinity for  $\text{CO}_2$  compared to  $\text{H}^+/\text{KPHI}$ . For  $\text{H}^+/\text{CaPHI}$  and  $\text{H}^+/\text{KPHI}$ , the extracted  $\Delta H_{\text{ads},A}$  in the primary sites were  $-42.2$  kJ  $\text{mol}^{-1}$  and  $-38.3$  kJ  $\text{mol}^{-1}$ ; in the weaker site, the  $\Delta H_{\text{ads},B}$  were  $-28.6$  and  $-23.7$  kJ  $\text{mol}^{-1}$ , respectively. The magnitudes for  $\Delta H_{\text{ads},A}$  while smaller than those typically encountered for chemisorptive mechanisms ( $>80$  kJ  $\text{mol}^{-1}$ ), were much larger than commonly measured for conventional physisorption which operates by pore filling alone ( $\sim 25$  kJ  $\text{mol}^{-1}$ ). Extracted  $\Delta H_{\text{ads},B}$  values, on the other hand, fall in this range expected for traditional physisorption mechanisms.

Additionally,  $\Delta G_{\text{ads},i}$  derived from the temperature-dependent dual site model were compared with the isosteric heats of adsorption ( $Q_{\text{st}}$ ) as quantified by the Clausius–Clapeyron relation (SI eq S5 and Figure S7).<sup>22</sup> The heats derived from the dual site analysis agreed well with the numerically calculated  $Q_{\text{st}}$  values, where the  $\Delta G_{\text{ads},A}$  matched with the  $Q_{\text{st}}$  observed at near-zero coverage of the surface with  $\text{CO}_2$ , while  $\Delta G_{\text{ads},B}$  corresponded with the plateau observed at larger  $\text{CO}_2$  loadings. The major difference between the  $\Delta G_{\text{ads},i}$  and  $Q_{\text{st}}$  was the shape of the curve; while the  $\Delta G_{\text{ads},i}$  derived from the dual-site fit shows a sharp transition between the two energetically distinct sites, the  $Q_{\text{st}}$  shows a smooth transition. Though the dual site model is useful in comparing the interaction of  $\text{CO}_2$  between the PHI frameworks, this discrepancy in the heat of adsorption curves suggests that, in reality, there is likely a continuum of sites with differing  $\text{CO}_2$  affinity in the PHI frameworks in contrast to the idealized assumptions of two constant energy sites in the DSL model. Despite this simplification of the energetic landscape implied by the DSL model, comparison of  $\Delta G_{\text{ads},i}$  with the  $Q_{\text{st}}$  from the Clausius–Clapeyron method gives credence to the dual site model and suggests that most of the relevant physics of the PHI- $\text{CO}_2$  system are captured.

In contrast to the large differences in  $\Delta H_{\text{ads},i}$  observed between the two adsorption sites, the  $\Delta S_{\text{ads},i}$  were of

comparable magnitude, differing only by about 5 J  $\text{mol}^{-1}$   $\text{K}^{-1}$  between the primary and secondary sites. For  $\text{H}^+/\text{CaPHI}$ , the  $\Delta S_{\text{ads},A}$  and  $\Delta S_{\text{ads},B}$  were  $-70.2$  and  $-65.1$  J  $\text{mol}^{-1}$   $\text{K}^{-1}$ , and for  $\text{H}^+/\text{KPHI}$ , the  $\Delta S_{\text{ads},A}$  and  $\Delta S_{\text{ads},B}$  were  $-65.9$  and  $-50$  J  $\text{mol}^{-1}$   $\text{K}^{-1}$ , respectively. These similar values of entropic losses likely indicate that the pore columns in the PHI architecture confine  $\text{CO}_2$  and restrict the translational and rotational motion to similar extents at both adsorption sites, despite the difference in enthalpic interactions. The slightly larger  $\Delta S_{\text{ads},i}$  could be indicative of a more restrictive environment in the  $\text{H}^+/\text{CaPHI}$  material, but further work on the exact physical mechanisms contributing to the entropic losses on gas adsorption in covalent frameworks are needed for a more comprehensive understanding. Overall,  $\text{H}^+/\text{CaPHI}$  exhibited both larger capacity and affinity for  $\text{CO}_2$  than  $\text{H}^+/\text{KPHI}$  in both adsorption sites despite their similar polymeric structure, which demonstrates the critical importance of the altered crystal structure and pore configuration for endowing  $\text{CO}_2$  adsorptive capacity.

In an attempt to further understand the nature of the strong interaction of  $\text{H}^+/\text{CaPHI}$  with  $\text{CO}_2$ , especially at low partial pressures, in situ ATR-FTIR was employed and the headspace was gradually exchanged from air to  $\text{CO}_2$ . Due to the relatively large values for  $\Delta H_{\text{ads},A}$  and presence of various types of amines in  $\text{H}^+/\text{CaPHI}$ , it was postulated that chemical interactions between  $\text{CO}_2$  and  $\text{H}^+/\text{CaPHI}$  might be discernible by ATR-FTIR. Indeed, amines are increasingly employed for capture of  $\text{CO}_2$  from dilute streams because of their large chemical affinity for  $\text{CO}_2$  during the formation of ionic carbamates, ammonium ions, and carbonates, and each of these moieties are visible by ATR-FTIR.<sup>23</sup> However, the in situ study shown in Figure 5b revealed that, even in the presence of significant partial pressures of  $\text{CO}_2$  (where a large quantity of  $\text{CO}_2$  adsorption is expected based on the acquired isotherm data), the IR signature of the PHI polymeric backbone was completely unchanged compared to that observed in ambient air. No peaks associated with chemisorption of  $\text{CO}_2$  by amines grew with time, and none of the peaks associated with the PHI backbone shifted in wavenumber. Instead, well-known peaks associated with the  $\nu_2$ ,  $\nu_3$ , and various combination modes of  $\text{CO}_2$ , associated with degenerate bending, asymmetric stretching, and Fermi resonance effects, were observed near 670, 2360, and 3600  $\text{cm}^{-1}$ , respectively. A blank measurement, shown in SI Figure S8, confirms that these features in the presence of the PHI framework show identical stretches as free  $\text{CO}_2$  molecules in the gas phase. The only change in the IR spectra associated with  $\text{H}^+/\text{CaPHI}$  was the small decrease in signal intensity of the N–H stretch around 3300  $\text{cm}^{-1}$ , which could be indicative of interaction of the structure-terminating primary amines with  $\text{CO}_2$ . However, as a whole, this in situ ATR FTIR data confirmed that, even in the presence of measurable quantities of  $\text{CO}_2$  where ample gas adsorption was expected, no covalent chemisorption interactions occurred, even with the stronger-affinity  $\text{H}^+/\text{CaPHI}$  framework. This conclusion agrees with the previous discussion of the heat of adsorption, as chemical reactivity is generally associated with much larger enthalpy changes. However, this IR data gives further concrete evidence that the adsorption mode of  $\text{CO}_2$  in the PHI, even for the primary high affinity site, can best be described as enhanced physisorption due to the highly polar surface that can interact with the polarizable  $\text{CO}_2$  via van der Waals interactions.

With concrete evidence against covalent interactions between the PHI framework and CO<sub>2</sub>, the large observed interaction energies could likely instead be associated with electrostatic effects. While CO<sub>2</sub> adsorption on conventional activated carbons is dominated by dispersive Lennard-Jones interactions due to their primarily nonpolar surfaces, zeolites with more ionic surfaces are well-known to exhibit strong adsorption affinity for CO<sub>2</sub>. We suspect that the carbon nitride allotropes studied here might exhibit adsorption modes closer to those observed for zeolites than for traditional carbon adsorbents that operate on physisorption alone. Indeed, Savateev et al. noted this structural similarity to zeolites, showing that KPHI crystals pack by “ionic self-assembly” by separating covalent and ionic entities in separated microphases, which results in the observed ordered pore channels and eclipsed heptazine columns.<sup>9</sup> When complexed to Ca<sup>2+</sup> or K<sup>+</sup>, the PHI frameworks effectively function as charged polyelectrolyte salts and contain a large quantity of ionic moieties. If these charge-separated moieties persist after H<sup>+</sup> exchange, these permanent dipoles and associated electric field gradients could help to explain the large  $\Delta H_{\text{ads,A}}$  observed for both H<sup>+</sup>/CaPHI and H<sup>+</sup>/KPHI. If this were the case, adsorption of CO<sub>2</sub> in the primary adsorption site ( $q_A$ ) could best be described as solvation of cation-type sites in the crystal structure by CO<sub>2</sub> molecules. Additionally, as Ca<sup>2+</sup> is a harder cation than K<sup>+</sup>, the increase in the adsorption enthalpy for H<sup>+</sup>/CaPHI compared to H<sup>+</sup>/KPHI could be related to residual effects in the electric field gradient resulting from the altered crystalline structure, as has been demonstrated previously for zeolites.<sup>24</sup> On the other hand, the weak adsorption in the secondary site ( $q_B$ ) would then be associated with physisorption in the frameworks’ ultramicroporosity. These physical assignments are consistent when considering the similarity in entropy losses associated with adsorption between the two sites, since both reside in the ordered pore channels within the PHI crystal structure. As both of these “active” adsorption sites occur in a cavity with similar nanoscale dimensions, the restriction to rotational motion (i.e., degrees of freedom) that directly contribute to the number of accessible microstates (i.e., entropy) would be similar, but the enthalpy of the sites could be very different when comparing to the cation type site vs physical adsorption/pore filling in the cavity after the cations had been saturated. While these speculations provide an additional level of interpretation, further in situ experiments outside the scope of the current work are required to definitively identify the adsorption modes and sites in these PHI frameworks.

In practice, ideal adsorbents for carbon capture from dilute streams should exhibit both large adsorption affinity and capacity for CO<sub>2</sub> at the partial pressure of interest. At the same time, an efficient separation process requires large selectivity of adsorption for CO<sub>2</sub> over other components of the feed stream.<sup>16</sup> In separation of CO<sub>2</sub> from flue gas or from air directly, the primary stream component is N<sub>2</sub> gas. Accordingly, N<sub>2</sub> isotherms were measured on H<sup>+</sup>/CaPHI and H<sup>+</sup>/KPHI at 30 °C and are shown in Figure 5a. Both materials show a near linear N<sub>2</sub> isotherm, indicating a smaller affinity toward N<sub>2</sub> than CO<sub>2</sub>. A comparison of the apparent Henry’s constants (estimated from the slopes at the isotherms near zero loading, SI Figure S9) for CO<sub>2</sub> and N<sub>2</sub> over H<sup>+</sup>/CaPHI and H<sup>+</sup>/KPHI provides an initial indication of the selectivity of adsorption, and H<sup>+</sup>/CaPHI and H<sup>+</sup>/KPHI showed Henry’s CO<sub>2</sub>/N<sub>2</sub> selectivities of 460 and 225, respectively. Though H<sup>+</sup>/KPHI showed a smaller quantity N<sub>2</sub> adsorption, the much larger

uptake of CO<sub>2</sub> at low pressures allowed for H<sup>+</sup>/CaPHI to maintain enhanced Henry’s selectivity compared to H<sup>+</sup>/KPHI. For more quantitative analysis of the adsorption selectivity, ideal adsorbed solution theory (IAST) was applied at various inlet gas compositions to predict the equilibrium loading of CO<sub>2</sub> and N<sub>2</sub> via the pyIAST algorithm developed by Simon et al.<sup>25</sup> For comparison, analogous analyses were performed on UTSA-16, a top-performing and water stable MOF that has recently been identified by detailed process simulations to achieve large CO<sub>2</sub> recovery, purity, and productivity with minimal energy costs in swing adsorption processes.<sup>26–30</sup> Predicted binary isotherms and resulting selectivities of the H<sup>+</sup>-exchanged carbon nitride frameworks are compared with those of UTSA-16 in Figure 6a,b and in SI Table S4. Additional comparisons against other benchmark adsorbents (viz., zeolite NaX and MOF Mg<sub>2</sub>(dobdc)) can also be found in the SI.

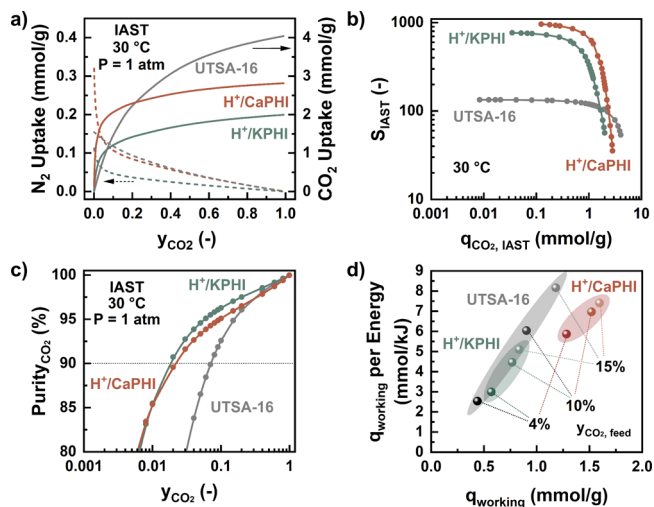


**Figure 6.** Estimates of selectivity, working capacity, and regeneration energy via (a) IAST-predicted binary adsorption isotherms at 30 °C, (b) adsorbed CO<sub>2</sub> loading vs IAST selectivity, (c) gas phase CO<sub>2</sub> concentration vs adsorbed phase purity, and (d) predicted working capacity and regeneration energy trade-off for a TSA process with various feed concentrations of CO<sub>2</sub>.

While UTSA-16 shows a larger overall CO<sub>2</sub> saturation capacity, larger pressures were required for significant CO<sub>2</sub> adsorption as compared to both H<sup>+</sup>/KPHI and H<sup>+</sup>/CaPHI. As shown in the IAST-predicted binary isotherms in Figure 6a, H<sup>+</sup>/CaPHI shows a steeper CO<sub>2</sub> uptake with comparable N<sub>2</sub> loading as UTSA-16. This larger CO<sub>2</sub> uptake at low feed concentrations of CO<sub>2</sub> resulted in nearly an order of magnitude increase in IAST selectivity for dilute streams, as visible in SI Figure S10. As the feed fraction of CO<sub>2</sub> increased, the selectivities of the PHI materials approached similar magnitude to UTSA-16. However, for various feed compositions relevant to postcombustion carbon capture for natural gas- or coal-fired flue gas (i.e., 4, 10, and 15%), the selectivity for both H<sup>+</sup>/KPHI and H<sup>+</sup>/CaPHI were about twice that of UTSA-16; at a feed concentration of 4% CO<sub>2</sub>, H<sup>+</sup>/KPHI, H<sup>+</sup>/CaPHI, and UTSA-16 exhibited IAST CO<sub>2</sub>/N<sub>2</sub> selectivities of 366, 303, and 124, respectively (SI Table S4). Adsorption selectivity has been shown to largely impact the overall cost of carbon capture, so these enhancements of selectivity with comparable CO<sub>2</sub> loading as indicated in Figure 6b demonstrate

the exceptional performance of these PHI adsorbents for efficient carbon capture from low-concentration streams.<sup>16,31</sup>

In addition to equilibrium loading and adsorption selectivity, performance in a given separation process is crucial for classifying and benchmarking adsorbents.<sup>32</sup> For example, regulatory committees have set a target for the purity of the resulting concentrated CO<sub>2</sub> as being above 90% for practical carbon capture and sequestration.<sup>33</sup> While full process simulation and optimization are out of the scope of the current work, useful estimates can be made to understand how the PHI adsorbents reported here compare to UTSA-16, which has been extensively studied. As such, Figure 6c reports the IAST-estimated purity of the adsorbed phase as a function of inlet gas composition. While the PHI materials are able to achieve the 90% purity target from streams with >2% CO<sub>2</sub>, higher concentrations (>7%) are required for similar performance from UTSA-16. In other words, these carbon nitride frameworks are applicable for CO<sub>2</sub> capture from dilute streams while top-performing UTSA-16 provides unsatisfactory performance. Besides purity, operating cost is another key metric that dictates the viability of a CO<sub>2</sub> separation process. Therefore, the working capacity and regeneration energy requirements for a temperature swing adsorption process were estimated with the model presented by Sculley et al. and the results are presented in Figure 6d and SI Figures S11 and S12.<sup>34</sup> Overall, while H<sup>+</sup>/KPHI shows comparable performance to UTSA-16 for selective CO<sub>2</sub> capture, H<sup>+</sup>/CaPHI shows superior CO<sub>2</sub> working capacity and adsorbed-phase purity with comparable required regeneration energy as compared to UTSA-16, especially at the dilute feed conditions relevant for practical carbon capture. This improvement in performance for H<sup>+</sup>/CaPHI compared to UTSA-16 is largely attributed to the difference in CO<sub>2</sub> isotherm shapes due to the relatively high enthalpy of adsorption of CO<sub>2</sub> in this covalent carbon nitride framework. Alongside comparable N<sub>2</sub> loadings, this increase in CO<sub>2</sub> uptake at relevant feed compositions more than doubles the adsorption selectivity for H<sup>+</sup>/CaPHI compared to UTSA-16.

## CONCLUSIONS

We report the discovery of a nanoporous framework material, CaPHI, that is an analogue to a previously studied allotrope of carbon nitride, KPHI. After extensive characterization by ATR-FTIR, MAS NMR, XPS, CHN analysis, XRD, electron microscopy, and DFT structure relaxation, the polymeric backbone, crystal structure, and band structure of CaPHI were determined. Replacement of K<sup>+</sup> with Ca<sup>2+</sup> during molten salt synthesis significantly altered the crystalline structure despite similar polymeric backbone, which resulted in a shift of the band structure and larger band gap for (H<sup>+</sup>/)CaPHI as compared to (H<sup>+</sup>/)KPHI. Porosimetry with N<sub>2</sub> adsorption showed that cation removal via protonation of both K- and CaPHI allowed considerable ultramicroporosity to be accessible for gas adsorption. Due to the crystal structure with nanoporous columns lined with fixed (partial) charges, these framework materials were investigated as adsorbents for selective CO<sub>2</sub> capture. Analysis of variable temperature CO<sub>2</sub> isotherms revealed a dual-site Langmuir adsorption mode for these carbon nitride frameworks. While both frameworks exhibited similar energetics of CO<sub>2</sub> adsorption, H<sup>+</sup>/CaPHI showed nearly twice as much CO<sub>2</sub> uptake at low pressures compared to H<sup>+</sup>/KPHI. Further, in situ ATR-FTIR revealed that the interaction of CO<sub>2</sub> with these frameworks, despite the

large observed isosteric heats of adsorption, is best described as enhanced physisorption (and not chemisorption). Performance of these adsorbents for a carbon capture process was estimated with predictions from IAST and with a simplified TSA model for comparison against top-performing MOF, UTSA-16, as well as other benchmark materials such as NaX and Mg<sub>2</sub>(dobdc). Proton-exchanged KPHI and CaPHI showed exceptional IAST CO<sub>2</sub>/N<sub>2</sub> selectivity of 366 and 303 at 4% CO<sub>2</sub> concentration compared to 124 for UTSA-16. This enhanced selectivity permits use of these PHI adsorbents for CO<sub>2</sub> capture from low concentration streams with appreciable estimated working capacity and moderate regeneration energy cost.

Overall, this study revealed the propensity for porous carbon nitride frameworks to exhibit highly selective CO<sub>2</sub> capture, especially from dilute streams. Future work will focus on quantifying water adsorption and mixture adsorption equilibria on these covalent heptazine frameworks. Further, this work demonstrated the modulation of crystal structure in covalent organic frameworks with similar polymeric backbones by changing the identity of a framework-complexed cation during synthesis. This dipole-rich, nanoporous carbon nitride framework with noteworthy carbon capture performance was synthesized in large yields from cheap and abundant precursors (i.e., urea and calcium chloride) and could likely be applied to other applications in sustainability, such as in mixed matrix membranes for gas separation or as a photocatalyst with strong oxidizing power.

## METHODS/EXPERIMENTAL

Melon-based carbon nitride (C<sub>3</sub>N<sub>4</sub>) was synthesized via thermal condensation of urea in air. Briefly, ~100 g of urea was ground and placed in an alumina crucible and wrapped tightly with aluminum foil before heating at 2.3 °C/min from room temperature to 550 °C in a benchtop muffle furnace (Neytech Vulcan 3-550) and held for 4 h before ambient cooling to yield ~10g of C<sub>3</sub>N<sub>4</sub>. The pale yellow, fluffy powder was ground in a mortar and pestle before further treatment.

KPHI was synthesized following the protocol established by Schlomberg et al.<sup>7</sup> Potassium thiocyanate (KSCN) was heated to 140 °C overnight in a vacuum oven (Lindberg Blue M, Thermo Scientific) to remove water. Briefly, 1.5 g of C<sub>3</sub>N<sub>4</sub> and 3 g of dried KSCN were ground in a mortar and transferred to an alumina crucible with a lid and placed in a tube furnace (OTF-1200X, MTI Corp.). Air in the furnace was displaced by Argon flow before heating the samples to 400 °C at 30 °C/min and holding for 1 h. After, the sample was again heated at 30 °C/min to 500 °C, held for 30 min, and subsequently cooled to ambient temperature naturally. The resulting bright yellow solid was ground and washed with 2 L of DI water by vacuum filtration to displace residual salt. The powder was dried in air at 120 °C overnight.

CaPHI was synthesized with a method modified from our previous work.<sup>11</sup> Briefly, 1.5 g of C<sub>3</sub>N<sub>4</sub> was ground together with 3 g of CaCl<sub>2</sub> and then sonicated for 5 min in ethanol. Ethanol was removed via evaporation in an oven at 120 °C overnight. The resulting impregnated C<sub>3</sub>N<sub>4</sub> was again ground then placed in an alumina crucible with a lid. The crucible was placed in a tube furnace under Ar atmosphere before heating to 700 °C at a rate of 10 °C/min. The sample was held at 700 °C for 2 h before ramping back down to 30 °C at a slow rate of 2 °C/min. After cooling, the sample was washed with 2 L of DI water by vacuum filtration to yield a light orange powder. Out of many tested synthetic protocols, this combination of salt ratio, hold time, and slow cooling rate was observed to result in the most crystalline sample. The powder was dried in air at 120 °C overnight.

H<sup>+</sup>/KPHI and H<sup>+</sup>/CaPHI were synthesized by stirring KPHI or CaPHI, respectively, in 1 M hydrochloric acid (HCl) overnight at

room temperature and subsequently washing with 2 L of DI water by vacuum filtration to yield a paler solid powder. These powders were dried in air at 120 °C overnight.

A complete description of additional material characterization, experimental, and analysis techniques can be found in the SI.

## ASSOCIATED CONTENT

### Supporting Information

The Supporting Information is available free of charge at <https://pubs.acs.org/doi/10.1021/acsnano.1c08912>.

Additional experimental and characterization details related to NMR, FTIR, XPS, UPS, UV-vis, XRD, electron microscopy, porosimetry, gas adsorption, elemental analysis, DFT, isotherm fitting, IAST analysis, and TSA predictions (PDF)

## AUTHOR INFORMATION

### Corresponding Author

C. Buddie Mullins – John J. McKetta Department of Chemical Engineering, Department of Chemistry, and Texas Materials Institute, The University of Texas at Austin, Austin, Texas 78712, United States; [orcid.org/0000-0003-1030-4801](https://orcid.org/0000-0003-1030-4801); Email: [mullins@che.utexas.edu](mailto:mullins@che.utexas.edu)

### Authors

James N. Burrow – John J. McKetta Department of Chemical Engineering, The University of Texas at Austin, Austin, Texas 78712, United States; [orcid.org/0000-0002-7445-3788](https://orcid.org/0000-0002-7445-3788)

Ryan A. Ciuffo – Department of Chemistry, The University of Texas at Austin, Austin, Texas 78712, United States

Lettie A. Smith – Department of Chemistry, The University of Texas at Austin, Austin, Texas 78712, United States; [orcid.org/0000-0003-0378-072X](https://orcid.org/0000-0003-0378-072X)

Yu Wang – Corporate Strategic Research, ExxonMobil Research and Engineering Company, Annandale, New Jersey 08801, United States; [orcid.org/0000-0002-3444-9207](https://orcid.org/0000-0002-3444-9207)

David C. Calabro – Corporate Strategic Research, ExxonMobil Research and Engineering Company, Annandale, New Jersey 08801, United States; [orcid.org/0000-0003-2424-3456](https://orcid.org/0000-0003-2424-3456)

Graeme Henkelman – Department of Chemistry and Texas Materials Institute, The University of Texas at Austin, Austin, Texas 78712, United States; [orcid.org/0000-0002-0336-7153](https://orcid.org/0000-0002-0336-7153)

Complete contact information is available at: <https://pubs.acs.org/10.1021/acsnano.1c08912>

### Notes

The authors declare no competing financial interest.

## ACKNOWLEDGMENTS

We thank ExxonMobil Research & Engineering and the Robert A. Welch Foundation (C.B.M, Grant No. F-1436; G.H., Grant No. F-1841) for their generous support of this research. J.N.B. also thanks the Sellers family for providing a graduate research fellowship; Dr. H. Celio for assistance with XPS/UPS; Prof. Z. Page and M. Allen for assistance with FTIR; and Prof. N. Peppas and A. Murphy for assistance with potentiometric titration.

## REFERENCES

- (1) Côté, A. P.; Benin, A. I.; Ockwig, N. W.; O’Keeffe, M.; Matzger, A. J.; Yaghi, O. M. Porous, Crystalline, Covalent Organic Frameworks. *Science*. **2005**, *310*, 1166–1170.
- (2) Kuhn, P.; Antonietti, M.; Thomas, A. Porous, Covalent Triazine-Based Frameworks Prepared by Ionothermal Synthesis. *Angew. Chem., Int. Ed.* **2008**, *47*, 3450–3453.
- (3) Krishnaraj, C.; Jena, H. S.; Leus, K.; Van Der Voort, P. Covalent Triazine Frameworks - a Sustainable Perspective. *Green Chem.* **2020**, *22*, 1038–1071.
- (4) Liu, M.; Guo, L.; Jin, S.; Tan, B. Covalent Triazine Frameworks: Synthesis and Applications. *J. Mater. Chem. A* **2019**, *7*, 5153–5172.
- (5) Zhang, G.; Li, G.; Lan, Z. A.; Lin, L.; Savateev, A.; Heil, T.; Zafeirotos, S.; Wang, X.; Antonietti, M. Optimizing Optical Absorption, Exciton Dissociation, and Charge Transfer of a Polymeric Carbon Nitride with Ultrahigh Solar Hydrogen Production Activity. *Angew. Chem., Int. Ed.* **2017**, *56*, 13445–13449.
- (6) Savateev, A.; Antonietti, M. Ionic Carbon Nitrides in Solar Hydrogen Production and Organic Synthesis: Exciting Chemistry and Economic Advantages. *ChemCatChem*. **2019**, *11*, 6166–6176.
- (7) Schlomberg, H.; Kröger, J.; Savasci, G.; Terban, M. W.; Bette, S.; Moudrakovski, I.; Duppel, V.; Podjaski, F.; Siegel, R.; Senker, J.; Dinnebier, R. E.; Ochsenfeld, C.; Lotsch, B. V. Structural Insights into Poly(Heptazine Imides): a Light-Storing Carbon Nitride Material for Dark Photocatalysis. *Chem. Mater.* **2019**, *31*, 7478–7486.
- (8) Chen, Z.; Savateev, A.; Pronkin, S.; Papaefthimiou, V.; Wolff, C.; Willinger, M. G.; Willinger, E.; Neher, D.; Antonietti, M.; Dontsova, D. The Easier the Better” Preparation of Efficient Photocatalysts-Metastable Poly(Heptazine Imide) Salts. *Adv. Mater.* **2017**, *29*, 1700555.
- (9) Savateev, A.; Pronkin, S.; Willinger, M. G.; Antonietti, M.; Dontsova, D. Towards Organic Zeolites and Inclusion Catalysts: Heptazine Imide Salts Can Exchange Metal Cations in the Solid State. *Chem. - Asian J.* **2017**, *12*, 1517–1522.
- (10) Sahoo, S. K.; Teixeira, I. F.; Naik, A.; Heske, J.; Cruz, D.; Antonietti, M.; Savateev, A.; Kü, T. D. Photocatalytic Water Splitting Reaction Catalyzed by Ion-Exchanged Salts of Potassium Poly(Heptazine Imide) 2D Materials. *J. Phys. Chem. C* **2021**, *125*, 13749–13758.
- (11) Burrow, J. N.; Pender, J. P.; Guerrero, J. V.; Wygant, B. R.; Eichler, J. E.; Calabro, D. C.; Mullins, C. B.; Mullins, C. B. CaCl<sub>2</sub>-Activated Carbon Nitride: Hierarchically Nanoporous Carbons with Ultrahigh Nitrogen Content for Selective CO<sub>2</sub> Adsorption. *ACS Appl. Nano Mater.* **2020**, *3*, 5965–5977.
- (12) Kumar, V.; Kr Sharma, S.; Sharma, T. P.; Singh, V. Band Gap Determination in Thick Films from Reflectance Measurements. *Opt. Mater. (Amst)*. **1999**, *12*, 115–119.
- (13) Chen, Y.; Wang, B.; Lin, S.; Zhang, Y.; Wang, X. Activation of n → π\* Transitions in Two-Dimensional Conjugated Polymers for Visible Light Photocatalysis. *J. Phys. Chem. C* **2014**, *118*, 29981–29989.
- (14) Jorge, A. B.; Martin, D. J.; Dhanoa, M. T. S.; Rahman, A. S.; Makwana, N.; Tang, J.; Sella, A.; Corà, F.; Firth, S.; Darr, J. A.; McMillan, P. F. H<sub>2</sub> and O<sub>2</sub> Evolution from Water Half-Splitting Reactions by Graphitic Carbon Nitride Materials. *J. Phys. Chem. C* **2013**, *117*, 7178–7185.
- (15) Savateev, A.; Tarakina, N. V.; Strauss, V.; Hussain, T.; ten Brummelhuis, K.; Sánchez Vadiello, J. M.; Markushyna, Y.; Mazzanti, S.; Tyutyunnik, A. P.; Walczak, R.; Oschatz, M.; Guldi, D. M.; Karton, A.; Antonietti, M. Potassium Poly(Heptazine Imide): Transition Metal-Free Solid-State Triplet Sensitizer in Cascade Energy Transfer and [3 + 2]-Cycloadditions. *Angew. Chem., Int. Ed.* **2020**, *59*, 15061–15068.
- (16) Oschatz, M.; Antonietti, M. A Search for Selectivity to Enable CO<sub>2</sub> Capture with Porous Adsorbents. *Energy Environ. Sci.* **2018**, *11*, 57–70.
- (17) Walton, K. S.; Abney, M. B.; LeVan, M. D. CO<sub>2</sub> Adsorption in Y and X Zeolites Modified by Alkali Metal Cation Exchange. *Microporous Mesoporous Mater.* **2006**, *91*, 78–84.

- (18) Mason, J. A.; Sumida, K.; Herm, Z. R.; Krishna, R.; Long, J. R. Evaluating Metal-Organic Frameworks for Post-Combustion Carbon Dioxide Capture via Temperature Swing Adsorption. *Energy Environ. Sci.* **2011**, *4*, 3030–3040.
- (19) Gargiulo, N.; Peluso, A.; Aprea, P.; Pepe, F.; Caputo, D. CO<sub>2</sub> Adsorption on Polyethylenimine-Functionalized SBA-15 Mesoporous Silica: Isotherms and Modeling. *J. Chem. Eng. Data* **2014**, *59*, 896–902.
- (20) Liu, Y. Is the Free Energy Change of Adsorption Correctly Calculated? *J. Chem. Eng. Data* **2009**, *54*, 1981–1985.
- (21) Sevilla, M.; Parra, J. B.; Fuertes, A. B. Assessment of the Role of Micropore Size and N-Doping in CO<sub>2</sub> Capture by Porous Carbons. *ACS Appl. Mater. Interfaces* **2013**, *5*, 6360–6368.
- (22) Nuhn, A.; Janiak, C. A Practical Guide to Calculate the Isothermic Heat/Enthalpy of Adsorption Via Adsorption Isotherms in Metal-Organic Frameworks, MOFs. *Dalton Trans.* **2020**, *49*, 10295–10307.
- (23) Wilfong, W. C.; Srikanth, C. S.; Chuang, S. S. C. In Situ ATR and DRIFTS Studies of the Nature of Adsorbed CO<sub>2</sub> on Tetraethylenepentamine Films. *ACS Appl. Mater. Interfaces* **2014**, *6*, 13617–13626.
- (24) Pham, T. D.; Hudson, M. R.; Brown, C. M.; Lobo, R. F. Molecular Basis for the High CO<sub>2</sub> Adsorption Capacity of Chabazite Zeolites. *ChemSusChem* **2014**, *7*, 3031–3038.
- (25) Simon, C. M.; Smit, B.; Haranczyk, M. PyIAST: Ideal Adsorbed Solution Theory (IAST) Python Package. *Comput. Phys. Commun.* **2016**, *200*, 364–380.
- (26) Xiang, S.; He, Y.; Zhang, Z.; Wu, H.; Zhou, W.; Krishna, R.; Chen, B. Microporous Metal-Organic Framework with Potential for Carbon Dioxide Capture at Ambient Conditions. *Nat. Commun.* **2012**, *3*, 1–9.
- (27) Masala, A.; Vitillo, J. G.; Bonino, F.; Manzoli, M.; Grande, C. A.; Bordiga, S. New Insights into UTSA-16. *Phys. Chem. Chem. Phys.* **2016**, *18*, 220–227.
- (28) Masala, A.; Vitillo, J. G.; Mondino, G.; Grande, C. A.; Blom, R.; Manzoli, M.; Marshall, M.; Bordiga, S. CO<sub>2</sub> Capture in Dry and Wet Conditions in UTSA-16 Metal-Organic Framework. *ACS Appl. Mater. Interfaces* **2017**, *9*, 455–463.
- (29) Burns, T. D.; Pai, K. N.; Subraveti, S. G.; Collins, S. P.; Krykunov, M.; Rajendran, A.; Woo, T. K. Prediction of MOF Performance in Vacuum Swing Adsorption Systems for Postcombustion CO<sub>2</sub> Capture Based on Integrated Molecular Simulations, Process Optimizations, and Machine Learning Models. *Environ. Sci. Technol.* **2020**, *54*, 4536–4544.
- (30) Farmahini, A. H.; Krishnamurthy, S.; Friedrich, D.; Brandani, S.; Sarkisov, L. Performance-Based Screening of Porous Materials for Carbon Capture. *Chem. Rev.* **2021**, *121*, 10666–10741.
- (31) Belmabkhout, Y.; Guillerm, V.; Eddaoudi, M. Low Concentration CO<sub>2</sub> Capture Using Physical Adsorbents: Are Metal-Organic Frameworks Becoming the New Benchmark Materials? *Chem. Eng. J.* **2016**, *296*, 386–397.
- (32) Rajagopalan, A. K.; Avila, A. M.; Rajendran, A. Do Adsorbent Screening Metrics Predict Process Performance? A Process Optimisation Based Study for Post-Combustion Capture of CO<sub>2</sub>. *Int. J. Greenh. Gas Control* **2016**, *46*, 76–85.
- (33) Shirley, P.; Myles, P. Quality Guidelines for Energy System Studies: CO<sub>2</sub> Impurity Design Parameters. *United States OSTI* **2019**, 1–27.
- (34) Sculley, J. P.; Verdegaa, W. M.; Lu, W.; Wriedt, M.; Zhou, H. C. High-Throughput Analytical Model to Evaluate Materials for Temperature Swing Adsorption Processes. *Adv. Mater.* **2013**, *25*, 3957–3961.

## Recommended by ACS

### Nitro-Decorated Microporous Covalent Organic Framework (TpPa-NO<sub>2</sub>) for Selective Separation of C<sub>2</sub>H<sub>4</sub> from a C<sub>2</sub>H<sub>2</sub>/C<sub>2</sub>H<sub>4</sub>/CO<sub>2</sub> Mixture and CO<sub>2</sub> Capture

Xiao-Hong Xiong, Zhang-Wen Wei, *et al.*

JULY 06, 2022

ACS APPLIED MATERIALS & INTERFACES

READ 

### Understanding the Ingenious Dual Role-Playing of CO<sub>2</sub> in One-Pot Pressure-Swing Synthesis of Linear Carbonate

Yuting He, Guofeng Guan, *et al.*

FEBRUARY 08, 2022

ACS SUSTAINABLE CHEMISTRY & ENGINEERING

READ 

### Construction of Hierarchical Porous Polycyanurate Networks with Cobaltoporphyin for CO<sub>2</sub> Adsorption and Efficient Conversion to Cyclic Di- and Tri-Carbonates

Gen Li, Zhonggang Wang, *et al.*

MAY 31, 2022

MACROMOLECULES

READ 

### Fabrication of Functionalized UiO-66 Anchored on Disorderly Layered Clinoptilolite via Surfactant-Assisted Induction for Selective Adsorption of CO<sub>2</sub> and CH<sub>4</sub>

Bingying Jia, Shiyang Bai, *et al.*

NOVEMBER 25, 2022

LANGMUIR

READ 

Get More Suggestions >